

3D-Printing Electrolytes for Solid-State Batteries

Dennis W. McOwen, Shaomao Xu, Yunhui Gong, Yang Wen, Griffin L. Godbey, Jack E. Gritton, Tanner R. Hamann, Jiaqi Dai, Gregory T. Hitz, Liangbing Hu,* and Eric D. Wachsman*

Solid-state batteries have many enticing advantages in terms of safety and stability, but the solid electrolytes upon which these batteries are based typically lead to high cell resistance. Both components of the resistance (interfacial, due to poor contact with electrolytes, and bulk, due to a thick electrolyte) are a result of the rudimentary manufacturing capabilities that exist for solid-state electrolytes. In general, solid electrolytes are studied as flat pellets with planar interfaces, which minimizes interfacial contact area. Here, multiple ink formulations are developed that enable 3D printing of unique solid electrolyte microstructures with varying properties. These inks are used to 3D-print a variety of patterns, which are then sintered to reveal thin, nonplanar, intricate architectures composed only of $\text{Li}_7\text{La}_3\text{Zr}_2\text{O}_{12}$ solid electrolyte. Using these 3D-printing ink formulations to further study and optimize electrolyte structure could lead to solid-state batteries with dramatically lower full cell resistance and higher energy and power density. In addition, the reported ink compositions could be used as a model recipe for other solid electrolyte or ceramic inks, perhaps enabling 3D printing in related fields.

Solid-state lithium conductors such as garnet-type $\text{Li}_7\text{La}_3\text{Zr}_2\text{O}_{12}$ (LLZ) have generated an enormous amount of interest as electrolytes for solid-state lithium batteries due to the key advantages these materials possess that could revolutionize battery technology. The first benefit is that they are generally safer nonflammable materials, unlike the volatile carbonate solvents and reactive lithium salts used in conventional Li-ion battery electrolytes that are known to be the main reason these batteries can catch fire.^[1–3] Second, many of the garnet-type lithium conductors have high electrochemical stability. LLZ in

particular is stable to lithium metal, the battery anode of choice—lithium metal has the highest specific capacity and the most negative redox potential of any electrode. However, lithium metal cannot be used in conventional Li-ion batteries with liquid electrolytes due to Li dendrite propagation, which short-circuits the cell leading to catastrophic failure.^[4–6] Without Li metal, batteries are limited in the energy density that can be achieved. Multiple researchers have demonstrated that Li metal can be cycled with LLZ solid electrolyte without dendrite propagation at moderate to high current densities using surface coatings to improve the Li/LLZ contact.^[3,7–10] Additionally, LLZ has also been shown to be stable to over 6 V^[11–13] and has successfully been cycled with various cathode materials in full cells, including LiCoO_2 , LiMn_2O_4 , and LiFePO_4 .^[10,11,14–17] Due to its remarkable


thermal and electrochemical stability, LLZ electrolyte could well be the material that is needed for the next breakthrough in Li battery technology. Other promising solid electrolytes, such as $\text{La}_{2/3-x}\text{Li}_{3x}\text{TiO}_3$ and $\text{Li}_{10}\text{GeP}_2\text{S}_{12}$, have different trade-offs but could also be used in solid-state batteries. For example, both materials can have a higher ionic conductivity than LLZ, but are not stable to lithium metal.^[18–20]

A main obstacle hindering the commercialization of LLZ and similar solid electrolytes in Li batteries is high cell area specific resistance (ASR), with contributions both from impedance of the thick electrolyte and interfacial impedance caused by poor electrode–electrolyte contact.^[10,17] The high impedance of the electrolyte is itself caused by two factors: relatively low conductivity and long diffusion distance. Reported conductivity values for LLZ-type garnet electrolytes can reach up to 1.0 mS cm^{-1} , while conventional inorganic liquid battery electrolytes are near 10 mS cm^{-1} , an order of magnitude higher.^[21,22] Furthermore, ceramic electrolytes less than $\approx 150 \text{ }\mu\text{m}$ thick are difficult to manufacture without advanced fabrication methods. In contrast, a typical separator thickness (and thus the liquid electrolyte “thickness”) in Li-ion batteries is $\approx 25 \text{ }\mu\text{m}$.^[23] With a significantly lower conductivity and longer diffusion path for the Li^+ cations to cross the cell, a high electrolyte impedance arises.

Poor electrode–electrolyte contact exacerbates the issue. While liquid electrolytes can wet and conform to the electrode

Dr. D. W. McOwen, Dr. S. Xu, Dr. Y. Gong, Dr. Y. Wen, G. L. Godbey, J. E. Gritton, T. R. Hamann, J. Dai, Dr. G. T. Hitz, Prof. L. Hu, Prof. E. D. Wachsman
Maryland Energy Innovation Institute
University of Maryland
College Park, MD 20742, USA
E-mail: binghu@umd.edu; ewach@umd.edu

Dr. D. W. McOwen, Dr. S. Xu, Dr. Y. Gong, Dr. Y. Wen, G. L. Godbey, J. E. Gritton, T. R. Hamann, J. Dai, Dr. G. T. Hitz, Prof. L. Hu, Prof. E. D. Wachsman
Department of Materials Science and Engineering
University of Maryland
College Park, MD 20742, USA

 The ORCID identification number(s) for the author(s) of this article can be found under <https://doi.org/10.1002/adma.201707132>.

DOI: 10.1002/adma.201707132

surface, solid electrolytes cannot, which drastically limits the total areal interface between the electrode and the electrolyte. Furthermore, garnet and other ceramic electrolytes are typically studied in flat, planar form—that is, the electrolyte powders are pressed into pellets and sintered to achieve uniform high density, which provides strength and high conductivity.^[7–9,11–17,24,25] However, the planar geometry of the pellets means that any interface with the electrodes is limited to only the geometric contact area. This factor in conjunction with the difficulty in achieving uniform solid–solid contact between the electrolyte and the electrodes contributes to the high interfacial impedance solid electrolytes are known for. Each of these factors contributes to a high resistance cell and severely limits the achievable current density in a battery to less than $50 \mu\text{A cm}^{-2}$, which will not be able to compete with standard liquid electrolyte Li-ion technology.^[8] Recently, researchers have begun to address this shortcoming by using polymer–ceramic composites to improve the electrode interface.^[26] In parallel, other groups have started to employ high porosity layers (uniform, random porosity) of solid electrolyte atop a thin, dense separating layer of the same material.^[10,27] The porous layers increase contact area with the electrodes significantly and act as a mechanical support, while the thin, high density separating layer maintains a short ion pathway across the cell, improving cell performance remarkably (e.g., lower impedance and much higher current density of 10 mA cm^{-2}).^[10] New solid electrolyte geometries are thus proven to be capable of addressing the high impedance problem of solid-state electrolytes. It has become apparent that what is now needed is a more thorough investigation of other solid electrolyte geometries and structures beyond planar or random porosity interfaces, and the subsequent optimization of these electrolyte structures to balance electrochemical and mechanical properties to determine the ideal cell configuration.

3D-printing technology is distinguished for its capability to rapidly explore different structure–property relationships at a wide range of length scales. In electrochemical applications, there have been numerous investigations using 3D printing to create uniquely shaped electrodes, with a particular focus on interdigitated electrode designs.^[28–31] However, the authors know of no reported study which reports 3D printing of a ceramic solid electrolyte. Solid electrolyte microstructures formed via 3D printing can enable a rapid investigation of interfacial structure–property relationships in solid-state electrochemical devices, similar to work that has been done for fuel cells.^[32,33] To that end, we have developed for the first time multiple solid electrolyte inks using LLZ garnet as a model solid electrolyte material. These inks are capable of printing micrometer-scale features and are tuned to create structures that range from being conformal to the surface of a substrate, creating a 5–10 μm sintered solid electrolyte film, to self-supporting, resulting in structures such as a stacked-array, or “log-cabin” type structure. These inks have a broad range of rheological properties that are manipulated by modifying the composition of the ink for a particular purpose, i.e., a desired rheological and/or structural property. In this report, a sampling of possible structures is printed and sintered revealing thin, and nonplanar, intricate architectures composed only of LLZ solid electrolyte. To demonstrate the efficacy of the garnet

inks, a symmetric Li|3D-printed LLZ|Li cell is cycled with low ASR. Using 3D printing to further study and optimize electrolyte structure could lead to solid-state batteries with dramatically lower full cell ASR and higher energy and power density. Many more designs and structures are possible with the inks developed in this work. The reported ink recipes could be easily modified to be used with other solid electrolyte or ceramic materials, perhaps enabling 3D printing in related fields.

Figure 1 shows an overview of cell fabrication using the 3D-printing process. This method is capable of printing a wide variety of ordered, high surface area LLZ structures, which can be challenging to produce at the lab scale with other methods for systematic study. Examples of these structures include lines, grids, columns, stacked arrays, or a combination (see Figures S1 and S2 in the Supporting Information for additional images of the printing process). The width of the printed features first depends on the size of the nozzle that is used in the print head, which ranges from 12.5 to 125 μm . The height of the features is then easily increased by printing additional layers. However, the exact shape of the printed features and how they connect to each other and the substrate is strongly dependent on the properties of ink itself. Specifically, the particle size, binder system, solvent blend, and fraction are critically important to the ink rheology and resulting structure type. In order to print micrometer-scale features, the solid electrolyte particles should ideally be more than an order of magnitude smaller than the desired feature width. Additionally, submicrometer particles are more easily dispersed and kept in suspension, which helps to keep the ink properties consistent throughout printing and storage. Particle size of the LLZ electrolyte can be reduced by simple ball milling, or by a sol–gel synthesis route. **Figure 2a** shows a typical particle size distribution (average particle size $\approx 300 \text{ nm}$) and scanning electron microscopy (SEM) image of the LLZ used for the inks.

To compose the inks, two binder systems were chosen, each of which has a different impact on the ink rheology and the properties of the dispensed ink. Polyvinyl butyral (PVB) binder with benzyl butyl phthalate (BBP) plasticizer is the first binder system, and ESL 441, a proprietary texanol-based composition, is the second binder system. As shown in Figure 2b,d, the rheology of the inks with the two binder systems is dramatically different. The PVB-BBP binder-based ink exhibits Newtonian behavior and has a viscosity of 1090 cP, although the viscosity can be easily modified by changing the amount of solvent in the ink (Figure 2e). The ESL binder-based ink exhibits fundamentally different Bingham plastic behavior with a yield stress of 280 Pa and a viscosity of 1500 cP. The Bingham plastic behavior is a result of the ESL binder system itself and causes the ink to retain its shape unless under high shear stress. The different characteristics of the binder systems can be exploited to generate different types of printed structures. The PVB-BBP binder system produces an ink that, due to its rheological behavior, partially wets and conforms to the surface it is printed on (**Figure 3d**). The PVB-BBP ink (hereafter referred to as the “conformal ink”) is well suited for printing thin, homogenous films of solid electrolyte due to its conformal nature and seamless joinery with other lines in the pattern. A demonstration of a $5 \times 5 \text{ cm}$ homogenous film printed using the conformal ink is shown in Figure 2f. By sintering a single layer of this film, a 5–10 μm free-standing highly uniform film has been achieved

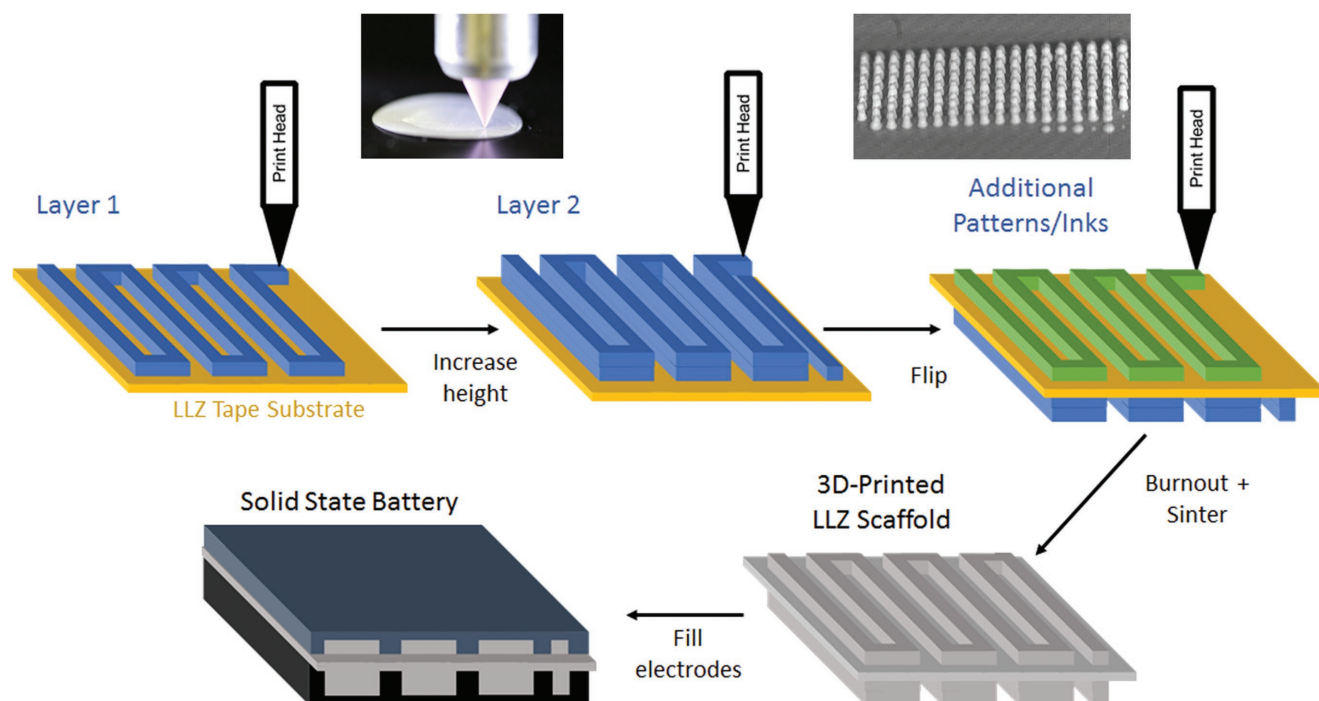


Figure 1. Schematic of the process to 3D-print solid electrolyte structures. In this case, the ink is printed on a LLZ substrate, which can be a 3D-printed LLZ film using the conformal ink, or an LLZ tape.^[10] The structure height is increased by adding layers, and different designs can be printed on either side of the substrate. Once dry, the 3D-printed LLZ inks and substrate are placed in a furnace for binder burnout and sintering, and are then ready for electrode infiltration to complete battery assembly.

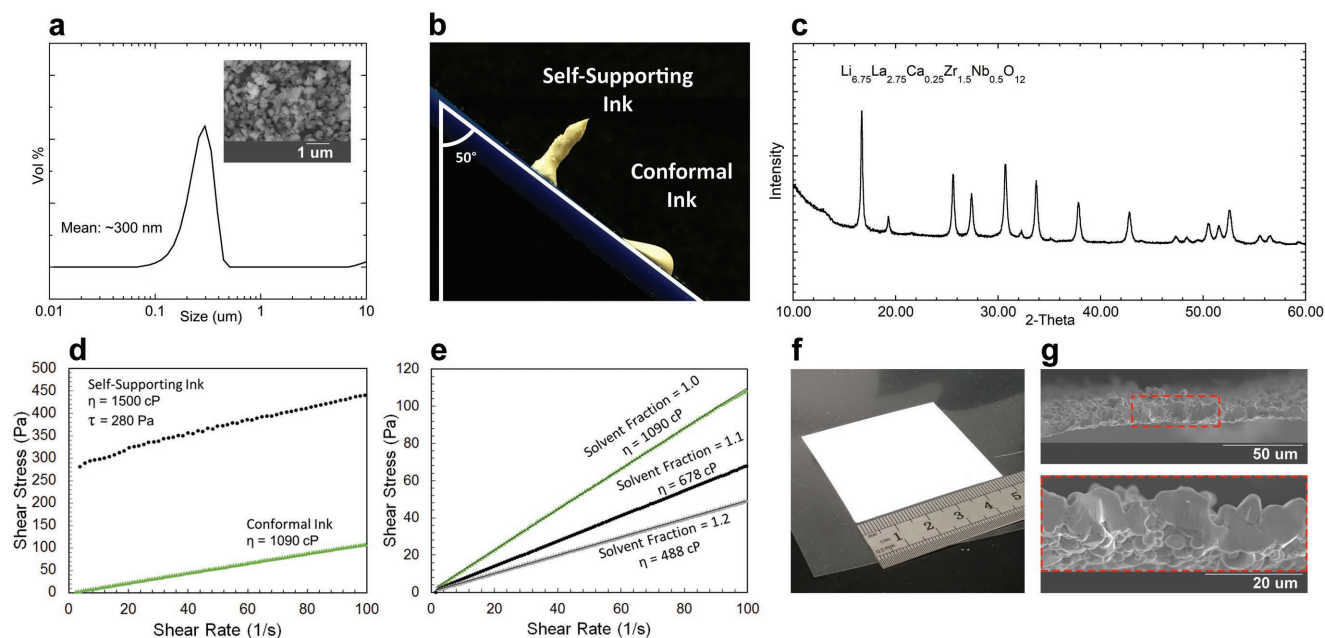


Figure 2. Properties of the LLZ powders and inks made from them. a) Particle size distribution and (inset) SEM image of sub-micrometer LLZ powder. b) Photograph of deposited inks that were tilted to $\approx 50^\circ$ demonstrating the stability of the self-supporting ink immediately after deposition. c) XRD of the LLZ used to make the inks showing pure cubic phase garnet. d) Rheological data for the self-supporting ink with a yield stress (τ) of 280 Pa and a viscosity of 1500 cP, contrasted with a conformal ink (green) with Newtonian behavior and a viscosity of 1090 cP. e) Rheological data for three conformal inks, controlling the viscosity by modifying the amount of solvent used: increasing normalized solvent fractions of 1.0 (green), 1.1 (black), and 1.2 (gray) corresponds with decreasing viscosity (η). f) Photograph of deposited single layer of conformal ink. g) SEM cross-sectional images of a single layer of ink with 5–10 μm thickness after sintering.

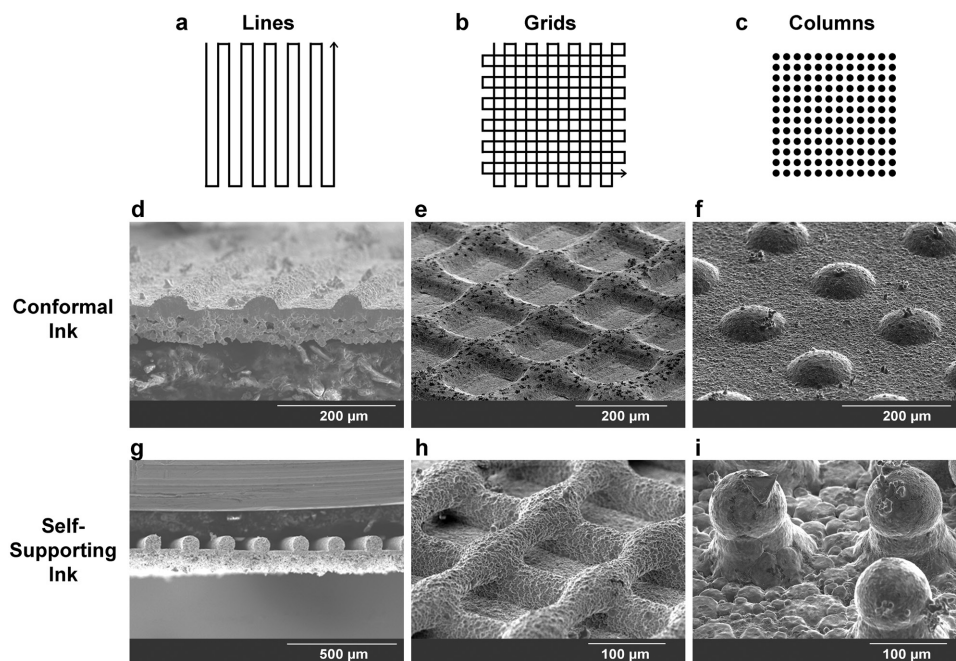


Figure 3. a–c) Diagrams and d–i) SEM images of 3D-printed LLZ microstructures comparing the 3D-printed conformal (d–f) and self-supporting (g–i) inks after sintering, including line (a,d,g), grid (b,e,h), and column (c,f,i) patterns. Each pattern was printed using similar printing scripts, with changes made to accommodate the different rheological properties of the inks (e.g., raster speed).

(Figure 2g) with high purity cubic-phase LLZ garnet (Figure 2c) and in most areas the film is only a single grain across. This demonstrates for the first time the ability to fabricate a dense layer of LLZ electrolyte that is $<10\text{ }\mu\text{m}$ without costly or low production volume thin film deposition methods (e.g., pulsed laser deposition, atomic layer deposition (ALD), etc.). A similar, more scalable tapecasting method that also used the PVB-BBP binder system recently achieved a $14\text{ }\mu\text{m}$ dense layer.^[10] A random porous-dense bilayer, such as that recently demonstrated by Hitz et al., can also be made by 3D printing with similar inks (Figure S3, Supporting Information).^[10] It is therefore possible to produce exceptionally thin, high-density LLZ electrolyte, which will help resolve the high impedance problem of solid-state batteries.

When used to create ordered structures, the conformal ink creates rounded lines or columns with a low aspect ratio (Figure 3d–f). This is due to the low viscosity and wetting nature of the ink. Another characteristic of the conformal ink is its ability to create seamless joints when printed lines intersect with each other (Figure 3e), which could be useful for creating high-strength structural members or increasing the number of ion conduction pathways.

Distinct from the conformal ink, the Bingham plastic behavior of the ESL binder ink creates structural features that maintain their shape immediately after printing (Figure 3g–i). Remarkably, subsequent printed layers of this ink (hereafter referred to as the “self-supporting” ink) are able to support themselves without sagging after printing and through the sintering process, as shown in Figure 3h,i that depicts the stacked array and column structures, respectively. When comparing similar designs printed with either the conformal ink (Figure 3d–f) or the self-supporting ink (Figure 3g–i), it is clear those printed with the self-supporting ink have a higher aspect ratio and thus

a higher surface area. For example, the aspect ratios of the line patterns printed with the conformal ink (Figure 3d) and the self-supporting ink (Figure 3g) are 0.37 and 0.83, respectively. The stacked-array structure has an additional increase in surface area due to the exposed area created by the bottom side of the second printed layer.

A wide variety of structures can be printed using only two different types of LLZ inks, possibly enabling a rapid investigation of the effect of electrolyte–electrode interface structural properties (tortuosity, surface area, etc.) on cell characteristics and performance. Although an in-depth study of the structure–performance relationships is outside the scope of this work, a symmetric cell made using the 3D-printed stacked array LLZ and lithium electrodes was fabricated to validate the efficacy of the 3D-printed electrolytes (Figure 4). An ALD coating was applied to both sides of the LLZ to allow wetting of the lithium to the LLZ surface.^[9] Figure 4a shows a diagram of the cell structure and Figure 4b shows a closeup of the lithium metal filling the pores of the LLZ stacked array structure. Intimate contact between the lithium and LLZ and increased contact area provided by the 3D-printed LLZ pattern ensure low lithium metal|LLZ electrolyte interfacial impedance. Figure S4 (Supporting Information) shows the EIS measurement of the cell before cycling, showing a low total ASR of $38\text{ }\Omega\text{ cm}^2$.

Figure 4c shows the symmetric DC cycling of the cell. The current density was varied from 0.1 to 0.33 mA cm^{-2} and back down to 0.1 mA cm^{-2} . The average overpotential at 0.1 and 0.33 mA cm^{-2} is 2.3 and 7.2 mV , both of which correspond to an ASR of $22\text{ }\Omega\text{ cm}^2$. This is lower than the measured EIS before cycling (Figure S4, Supporting Information), likely due to improved interfacial contact as the cell began cycling. When the current density was reduced back to 0.1 mA cm^{-2} , the average

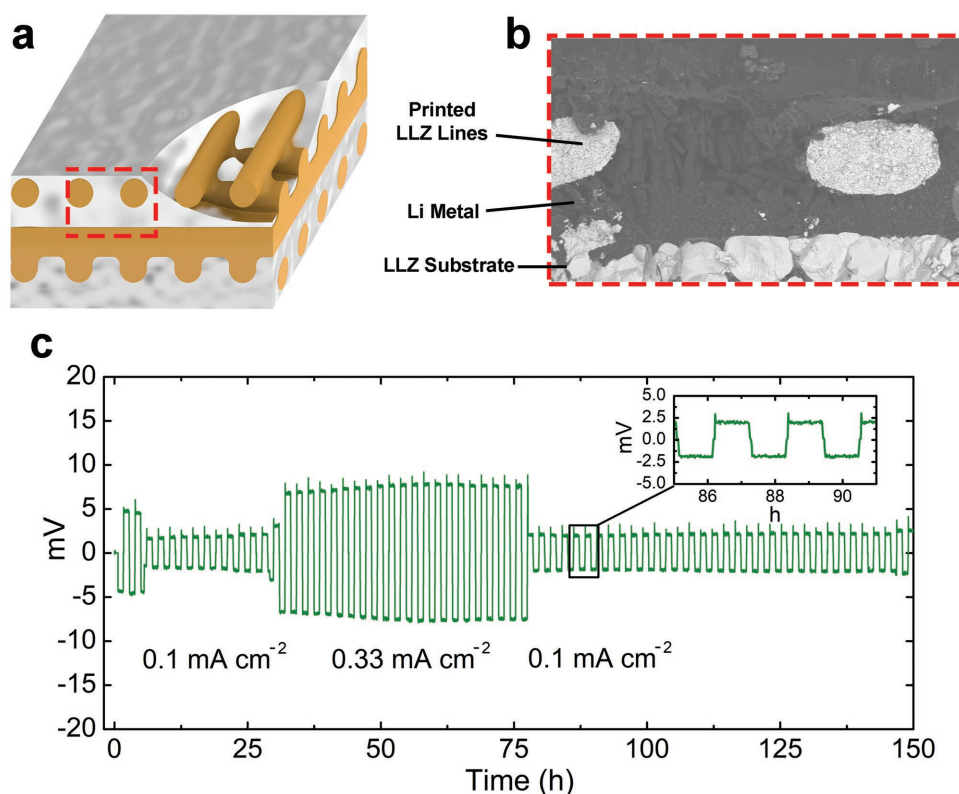


Figure 4. a) Schematic of Li-filled pores between 3D-printed LLZ grids in a stacked-array pattern on LLZ substrate. b) Cross-sectional SEM of 3D-printed LLZ/Li metal interface (red line). c) DC cycling of Li|3D-printed LLZ|Li metal cell at varying current densities. Each plating/stripping cycle was 1 h long.

overpotential decreased back to 2.0 mV, which also equates to an ASR of 20 Ω cm². The constant cycling ASR, independent of current density, demonstrates the high conductivity of the 3D-printed LLZ (Figure S5, Supporting Information). Furthermore, because the Li|LLZ interfacial impedance is negated by the ALD coating,^[9] the extremely low ASR also indicates the connections between all of the 3D-printed LLZ layers are seamless. Thus, the 3D-printed LLZ creates a continuous and multi-layer ordered electrolyte architecture that maintains the ability to block dendrite propagation and the high conductivity that is characteristic of the LLZ electrolyte.

The results discussed in this report demonstrate the ability to 3D-print LLZ solid electrolyte with the same properties as LLZ pellets produced through other methods. The ability to 3D-print solid electrolytes makes fabrication of unique ordered structures possible, whereas die-pressing and tape-casting methods are limited to planar geometries and random porosities. Two types of LLZ 3D-printable inks have been developed for different structural purposes, each of which can be further tailored by making minor changes to the ink composition. Using the “conformal” and “self-supporting” inks, a wide variety of different structures can be created and explored, from uniform films to columns to stacked “log-cabin” type structures. It is important to note that these ink compositions are not unique to LLZ and could be used as a starting recipe for printing other ceramic materials. These inks open a new realm of study for solid electrolytes, one in which the effect of 3D electrolyte architectures on electrochemical and mechanical properties (i.e.,

electrode/electrolyte interfacial contact, cell impedance and mechanical strength) can be explored and optimized, helping to make safe, high-energy density solid-state batteries a reality.

Experimental Section

LLZ Synthesis: Ca and Nb-doped Li₇La₃Zr₂O₁₂ garnet was made by solid-state synthesis or sol-gel method as previously described.^[9,10] For the solid-state synthesis, stoichiometric amounts of La₂O₃ (GFS Chemicals, 99.9%), ZrO₂ (Inframmat Advanced Materials), CaCO₃ (Carolina, Laboratory Grade), Nb₂O₅ (Alfa Aesar, 99.9%), and 10% excess LiOH·H₂O (Alfa Aesar, 98%) were milled for 1 d with 5 mm diameter Y₂O₃-stabilized ZrO₂ (YSZ) grinding media in isopropanol. The precursors were then dried and calcined at 900 °C. Phase analysis by X-ray diffraction is shown in Figure 2c. To achieve the desired particle size, calcined powder was milled in isopropanol with 5 mm YSZ grinding media followed by 2 mm media to further reduce particle size below 1 μ m. For the sol-gel method, stoichiometric amounts of La(NO₃)₃ (99.9%, Alfa Aesar), ZrO(NO₃)_x (99.9%, Alfa Aesar), LiNO₃ (99%, Alfa Aesar), NbCl₅ (99.99%, Alfa Aesar), and Ca(NO₃)₂ (99.9%, Sigma Aldrich) were dissolved in de-ionized water and 5 wt% excess LiNO₃ was added to compensate for lithium volatilization during the high-temperature processes. The precursors were calcined at 800 °C for 10 h and ball milled for 48 h in 200-proof ethanol to obtain cubic phase garnet powder (mean particle size 300 nm). Powders produced from each method were characteristically similar.

Ink Composition: For the “conformal ink,” LLZ powder (37%) was first mixed with a small amount of blown menhaden fish oil (Z-3, Tape Casting Warehouse, Inc.) as dispersant in a 7:3 mixture of *n*-butanol (99%, Alfa Aesar): α -terpineol (96%, Alfa Aesar) for 24 h on a vibratory mill with 5 mm YSZ media. Once the mixture was homogenous, PVB binder

(B-98, Tape Casting Warehouse, Inc.) and BBP plasticizer (S-160, Tape Casting Warehouse, Inc.) were added in a 1.6:1 weight ratio to give a total solids loading of 30%. The ink was mixed in a vibratory mill for 24 h before printing.

The “self-supporting ink” was created by first producing a dilute suspension composed of 20% garnet powder, 10% Electro Science Lab (ESL) 441 texanol-based binder system, and 70% 200-proof ethanol and ball milled for 24 h to disperse the garnet powder using 2 mm YSZ media. After ball milling, the suspension was transferred to a 250 mL HDPE jar in a Thinky mixer and mixed at 1500 rpm to vaporize the solvent to the desired solvent fraction and create the printing slurry.

3D Printing: The inks were printed with an nScript 3Dn-300 printer with two equipped SmartPumps and ceramic nozzles with nozzle diameter of 12.5, 25, or 125 μm . For uniform, homogenous film fabrication (Figure 2f,g), the inks were printed on a Mylar sheet. To print the ordered structures the inks were printed on a porous-dense multilayer LLZ tape substrate described previously^[10] for structural support and is characteristically identical to the 3D-printed uniform films. In all cases, the printing stage was heated to 30–35 °C to facilitate the drying process. The 3D-printed structures were then sintered in a tube furnace in a bed of mother powder, similar to the sintering method described elsewhere.^[10]

Material Characterization: Phase characterization of the LLZ powder was performed at the University of Maryland's X-ray Crystallography Center using a Bruker D8 X-ray diffractometer. Particle size data were collected for dilute solutions of LLZ in *N*-methyl-2-pyrrolidinone solvent and Triton X-100 dispersant using a Horiba Partica LA-950 Laser Diffraction Particle Size Distribution Analyzer. Rheology data were collected using a TA Instruments DHR-2 Rheometer at 25 °C from 1 to 100 Hz. A Hitachi SU-70 SEM in the UMD AIMLab and a Hitachi S-3400 SEM in the UMD FabLab were used for imaging of the LLZ powder and sintered LLZ 3D-printed layers.

Li Infiltration and Symmetric Cell Testing: Sintered 3D-printed LLZ layers were first treated with an ALD surface coating to improve Li wetting and interfacial contact of the Li metal to the LLZ electrolyte.^[9,10] Li metal was then coated on both sides of the LLZ structures by melting at 200 °C in an Ar glove box. The symmetric cell was packaged with stainless steel current collectors in a coin cell for testing on a Biologic VMP3 potentiostat. Cells were cycled at 0.10–0.33 mA cm⁻² for 1 h at room temperature.

Supporting Information

Supporting Information is available from the Wiley Online Library or from the author.

Acknowledgements

D.W.M. and S.X. contributed equally to this work. The authors gratefully acknowledge support by the NASA Advanced Energy Storage Systems Project (Contract No. NNC16CA03C) as part of the Game-Changing Development Program of the Space Technology Mission Directorate and by the DOE Energy Efficiency and Renewable Energy Battery 500 Consortium (Contract No. DEEE0008201). The authors thank the FabLab, AIMLab, and X-Ray Crystallography Center within the University of Maryland for their characterization tools. The authors also thank the Christopher M. Jewell Research Lab for use of its Horiba Particle Size Analyzer and Jim Andorko for his assistance.

Conflict of Interest

Eric D. Wachsman, Liangbing Hu, and Gregory T. Hitz founded a company to commercialize solid-state batteries. However, all results

reported herein were performed at the University of Maryland under federal sponsorship.

Keywords

3D printing, additive manufacturing, lithium metal, solid electrolytes, solid-state batteries

Received: December 6, 2017

Revised: January 25, 2018

Published online:

- [1] P. G. Balakrishnan, R. Ramesh, T. Prem Kumar, *J. Power Sources* **2006**, 155, 401.
- [2] Q. Wang, P. Ping, X. Zhao, G. Chu, J. Sun, C. Chen, *J. Power Sources* **2012**, 208, 210.
- [3] C. L. Campion, W. Li, B. L. Lucht, *J. Electrochem. Soc.* **2005**, 152, A2327.
- [4] J. R. Owen, *Chem. Soc. Rev.* **1997**, 26, 259.
- [5] J.-M. Tarascon, M. Armand, *Nature* **2001**, 414, 359.
- [6] J. Wen, Y. Yu, C. Chen, *Mater. Express* **2012**, 2, 197.
- [7] W. Luo, Y. Gong, Y. Zhu, K. K. Fu, J. Dai, S. D. Lacey, C. Wang, B. Liu, X. Han, Y. Mo, E. D. Wachsman, L. Hu, *J. Am. Chem. Soc.* **2016**, 138, 12258.
- [8] A. Sharafi, H. M. Meyer, J. Nanda, J. Wolfenstine, J. Sakamoto, *J. Power Sources* **2016**, 302, 135.
- [9] X. Han, Y. Gong, K. Fu, X. He, G. T. Hitz, J. Dai, A. Pearse, B. Liu, H. Wang, G. Rubloff, Y. Mo, V. Thangadurai, E. D. Wachsman, L. Hu, *Nat. Mater.* **2017**, 16, 572.
- [10] G. T. Hitz, D. W. McOwen, L. Zhang, Z. Ma, Z. Fu, Y. Wen, Y. Gong, J. Dai, T. R. Hamann, L. Hu, E. D. Wachsman, unpublished.
- [11] S. Ohta, T. Kobayashi, T. Asaoka, *J. Power Sources* **2011**, 196, 3342.
- [12] S. Kumazaki, Y. Iriyama, K.-H. Kim, R. Murugan, K. Tanabe, K. Yamamoto, T. Hirayama, Z. Ogumi, *Electrochem. Commun.* **2011**, 13, 509.
- [13] Y. Li, J.-T. Han, C.-A. Wang, H. Xie, J. B. Goodenough, *J. Mater. Chem.* **2012**, 22, 15357.
- [14] T. Kato, T. Hamanaka, K. Yamamoto, T. Hirayama, F. Sagane, M. Motoyama, Y. Iriyama, *J. Power Sources* **2014**, 260, 292.
- [15] S. Ohta, T. Kobayashi, J. Seki, T. Asaoka, *J. Power Sources* **2012**, 202, 332.
- [16] S. Ohta, S. Komagata, J. Seki, T. Saeki, S. Morishita, T. Asaoka, *J. Power Sources* **2013**, 238, 53.
- [17] M. Kotobuki, H. Munakata, K. Kanamura, Y. Sato, T. Yoshida, *J. Electrochem. Soc.* **2010**, 157, A1076.
- [18] S. Stramere, V. Thangadurai, W. Weppner, *Chem. Mater.* **2003**, 15, 3974.
- [19] P. Knauth, *Solid State Ionics* **2009**, 180, 911.
- [20] S. Wenzel, S. Randau, T. Leichtweiß, D. A. Weber, J. Sann, W. G. Zeier, J. Janek, *Chem. Mater.* **2016**, 28, 2400.
- [21] C. Devianapoorani, L. Dhiya, S. Ramakumar, R. Murugan, *J. Power Sources* **2013**, 240, 18.
- [22] K. Xu, *Chem. Rev.* **2014**, 114, 11503.
- [23] S. S. Zhang, *J. Power Sources* **2007**, 164, 351.
- [24] C.-W. Ahn, J.-J. Choi, J. Ryu, B.-D. Hahn, J.-W. Kim, W.-H. Yoon, J.-H. Choi, J.-S. Lee, D.-S. Park, *J. Power Sources* **2014**, 272, 554.
- [25] L. Cheng, C. H. Wu, A. Jarry, W. Chen, Y. Ye, J. Zhu, R. Kostecki, K. Persson, J. Guo, M. Salmeron, G. Chen, M. Doeff, *ACS Appl. Mater. Interfaces* **2015**, 7, 17649.
- [26] X. Tao, Y. Liu, W. Liu, G. Zhou, J. Zhao, D. Lin, C. Zu, O. Sheng, W. Zhang, H.-W. Lee, Y. Cui, *Nano Lett.* **2017**, 17, 2967.

- [27] J. van den Broek, S. Afyon, J. L. M. Rupp, *Adv. Energy Mater.* **2016**, 6, 1600736.
- [28] K. Sun, T.-S. Wei, B. Y. Ahn, J. Y. Seo, S. J. Dillon, J. A. Lewis, *Adv. Mater.* **2013**, 25, 4539.
- [29] C. C. Ho, J. W. Evans, P. K. Wright, *J. Micromech. Microeng.* **2010**, 20, 100409.
- [30] C. Zhao, C. Wang, R. GorkinIII, S. Beirne, K. Shu, G. G. Wallace, *Electrochem. Commun.* **2014**, 41, 20.
- [31] G. Sun, J. An, C. K. Chua, H. Pang, J. Zhang, P. Chen, *Electrochem. Commun.* **2015**, 51, 33.
- [32] J. R. Smith, A. Chen, D. Gostovic, D. Hickey, D. Kunder, K. L. Duncan, R. T. DeHoff, K. S. Jones, E. D. Wachsman, *Solid State Ionics* **2009**, 180, 90.
- [33] D. Gostovic, J. R. Smith, D. P. Kunder, K. S. Jones, E. D. Wachsman, *Electrochem. Solid-State Lett.* **2007**, 10, B214.